Figure 5. Osteophyte formation in the medial portion of tibial cartilage of wild-type (WT), $Runx2^{+/-}$, and $Runx2^{+/lacZ}$ mice 12 weeks after induction of joint instability. **A,** Representative anteroposterior radiographs. **B,** Representative histologic features of frontal sections (Safranin O staining). Boxed areas in the top row indicate the regions shown at higher magnification in the bottom row. Bars = 200 μm (top) and 50 μm (bottom). **C,** Histologic scoring of osteophyte formation according to the grading system described in Materials and Methods. **D,** Histomorphometric measurements of trabecular bone volume (bone volume/tissue volume [BV/TV]) in the subchondral region of medial tibial joints. Data in **C** and **D** are expressed as the mean and SEM of 10 samples per genotype per time for wild-type and $Runx2^{+/-}$ mice, and of 4 samples per time for $Runx2^{+/LacZ}$ mice. * = $P < 0.01$ versus wild-type mice.

phyte formation. Quantification by the osteophyte formation score (10) at 12 weeks confirmed the reduction by RUNX-2 insufficiency (Figure 5C). The trabecular bone volume in the subchondral region tended to be lower in mice with RUNX-2 insufficiency, although not statistically significant (Figure 5D). These findings demonstrate that RUNX-2 contributes to at least 2 characteristic features of OA: cartilage destruction and osteophyte formation under the unstable joint.

DISCUSSION

Although several studies have examined the expression of matrix proteins in OA cartilage using experimental models in larger animals, such as dogs and rabbits (3–7,9), the results have been inconsistent. For example, in rabbit models 1 study showed no alteration of CII expression (7), while another showed its up-regulation at region-specific sites (5). In canine models, CII expression was higher in OA knee joints, and expression progressed in one study (4) and decreased in another one (6). Other matrix proteins, such as aggrecan and fibromodulin, seem to be altered only at isolated time points (5,7).

Our previous immunohistochemical analyses using an experimental mouse OA model (medial model) showed no substantial change in CII, type IX collagen, MMP-2, MMP-3, or MMP-9 expression, but up-regulation of type X collagen and MMP-13 (10). The present time course analyses using the same model confirmed up-regulation of type X collagen and MMP-13 with no alteration of CII, by immunohistochemical and real-time RT-PCR analyses. In this model, definite increases in RUNX-2, type X collagen, and MMP-13 were seen at 2, 4, and 8 weeks, respectively, after surgery (Figures 1 and 2), while cartilage destruction became visible at 8 weeks (10). In addition, RUNX-2 insufficiency caused a decrease in cartilage destruction, along with a reduction in type X collagen and MMP-13 expression. Furthermore, transgenic mice expressing constitutively active MMP-13 are reported to exhibit articular cartilage destruction resembling OA (28). These findings indicate that induction of these molecules is the cause, not the effect, of the cartilage destruction.

Under physiologic conditions, articular cartilage does not show chondrocyte hypertrophy, but maintains the stable phenotype as a permanent cartilage. However, in OA articular cartilage, pathologic expression of type X collagen and other differentiation markers, including annexin VI, alkaline phosphatase, osteopontin, and osteocalcin, have been reported (11,12,29–31), indicating that OA articular cartilage cannot maintain the characteristics of the permanent cartilage, but gains those of the growth plate cartilage, which undergoes endochondral ossification. MMP-13, which potently degrades cartilage matrix with a preference for CII, is known to be induced in OA articular cartilage (32) and to be functionally involved in OA pathogenesis (28). This proteinase has been suggested to be induced in response to proinflammatory cytokines such as tumor necrosis factor

α (TNFα), interleukin-1 (IL-1), and IL-6 in articular cartilage under pathologic conditions, such as OA and rheumatoid arthritis (RA) (2,33). However, it is suspicious that these cytokines play significant roles in the development of OA. Our previous study showed that levels of TNFα, IL-1, IL-6, as well as fibroblast growth factor 2, in the synovial fluid from knee joints of patients with OA were much lower than those from patients with RA (34).

Furthermore, a recent study using a mouse OA model similar to ours (35) showed that mice lacking IL-1, IL-1β–converting enzyme, stromelysin 1, or inducible nitric oxide synthase unexpectedly exhibited an acceleration of cartilage destruction, implying that these proinflammatory factors do not stimulate, but rather inhibit, cartilage destruction. Instead, we propose that chondrocyte hypertrophy is important for MMP-13 induction in cartilage. There are well-ordered expression patterns of type X collagen and MMP-13 in the growth plate cartilage; only the highly differentiated cells in the type X collagen–positive hypertrophic chondrocytes are able to express MMP-13 (10,36,37). This sequence of expression may be essential for endochondral ossification that needs prior degradation of the cartilage matrix. The present time-course study also showed that MMP-13 expression occurred later than hypertrophic differentiation of OA chondrocytes, suggesting the principal role of chondrocyte hypertrophy in the development of OA.

Although several signaling molecules, including Indian hedgehog and parathyroid hormone–related peptide, have been shown in mouse genetics studies to regulate chondrocyte hypertrophy, RUNX-2 is known to be the only transcription factor that is necessary for hypertrophy, based on several lines of evidence. Runx2$^{-/-}$ mice show no hypertrophic chondrocytes in some skeletal elements (15,16), and expression of a dominant-negative *Runx2* mutation inhibits chondrocyte hypertrophy and ossification in vivo (18). Constitutive expression of RUNX-2 in prehypertrophic chondrocytes leads to premature and ectopic chondrocyte hypertrophy (17–19). In addition, endogenous RUNX-2 is known to be expressed mainly in prehypertrophic chondrocytes during endochondral ossification in skeletal development and growth (15,19). The present analysis also showed that RUNX-2 expression reached a maximum at 2–4 weeks and decreased at 8 weeks, suggesting that RUNX-2 is expressed in prehypertrophic chondrocytes that undergo hypertrophic differentiation and apoptosis thereafter in the OA cartilage as well.

The fact that type X collagen was induced shortly after RUNX-2 during OA progression is consistent with a recent finding that type X collagen is a direct transcriptional target of RUNX-2 by transactivation of the promoter (20). However, the time lag between RUNX-2 and MMP-13 expression was inconsistent with previous reports showing the direct activation of MMP-13 transcription by RUNX-2 (26,27). RUNX-2 may therefore induce type X collagen expression directly, and then the hypertrophic chondrocytes express MMP-13 during the development of OA.

The mechanism whereby mechanical instability induces RUNX-2 expression in articular cartilage remains unclarified. RUNX-2 was recently reported to be a target of mechanical signals, mainly in osteoblasts, causing anabolic action in bone. Low-level stretching, as well as extracellular nucleotides released in response to mechanical stimuli, up-regulates not only RUNX-2 expression, but also its DNA binding activity in cultured osteoblasts (38,39). This effect in bone was shown to be modulated by activation of ERK MAPK and protein kinase C.

In contrast, more complicated mechanoresponsive mechanisms appear to evolve in chondrocytes. Although tensile strain increased RUNX-2 expression, hydrostatic pressure decreased it somewhat in cultured primary chondrocytes (40). In fact, our preliminary experiment using the culture of chondrocytes isolated from the growth plate of wild-type and Runx2$^{+/-}$ mice, as described previously (41), failed to show induction of RUNX-2 by stretching stimulation using the Flexercell culture system (data not shown). Since we also could not find RUNX-2 induction in OA superficial chondrocytes earlier than 2 weeks after surgery (data not shown), it is likely that the induction is not directly from mechanical instability, but occurs by way of changes in other molecules. Establishment of a chondrocyte culture system that accurately reproduces the in vivo environment of OA articular cartilage induced by joint instability will be essential to elucidate the molecular network mediating RUNX-2 expression.

Accumulation of mechanical loading and the subsequent cartilage destruction were confined to the medial portion of the tibial cartilage in the present model, and the changes in RUNX-2, type X collagen, and MMP-13 were detected mainly in the affected medial portion. However, a previous study (9) has shown that expression levels of CII, type I collagen, and YKL-40 were up-regulated independently of joint localization during the early stages in an experimental canine OA model (3). Another study of expression levels of CII, aggrecan, biglycan, decorin, fibromodulin, and MMPs 1,

3, and 13 demonstrated significant region-specific changes in a rabbit OA model (5). Although the present study failed to detect the up-regulation of RUNX-2, type X collagen, or MMP-13 in the unaffected lateral portion, further studies of region-specific expression of a subset of transcription factors, cytokines, matrix molecules, proteinases, and proteinase inhibitors should elucidate the molecular network underlying the OA pathogenesis in the whole joint.

Although OA has long been considered to be primarily a cartilage disorder associated with focal articular cartilage degradation, recent studies suggest the involvement of subchondral trabecular bone in the pathophysiology (8,42,43). The increased subchondral bone stiffness is suggested to reduce the ability to dissipate the load and distribute the strain generated within the joint, which augments peak dynamic forces in the overlying articular cartilage and can accelerate its damage over time. In fact, the present study showed a decrease in the subchondral trabecular bone volume in mice with RUNX-2 insufficiency, although it was not statistically significant. Considering that *Runx2* is originally known as a master gene for bone formation, we cannot deny the possibility that reduced cartilage destruction due to RUNX-2 insufficiency is at least partly secondary to the decreased subchondral bone. Further analyses using bone- and cartilage-specific RUNX-2–deficient mice driven by type I collagen and CII promoters, respectively, would determine the tissue-specific role of RUNX-2 during OA progression.

We herein propose a mechanism of OA development, in which RUNX-2 expression induced by mechanical instability causes pathologic hypertrophic differentiation of articular chondrocytes, which then produces MMP-13 that degrades cartilage matrix. We certainly do not think that MMP-13 is the sole proteinase for cartilage degradation in OA. In fact, deletion of active ADAMTS-5 (aggrecanase 2), another member of the metalloproteinase family, was recently reported to prevent cartilage destruction in mouse arthritis models (44,45). We speculate that the cartilage degradation by these metalloproteinases may lead to osteophyte formation through endochondral ossification at the edge of the articular cartilage to which new blood vessels are accessible by adjacent synovial or fibrous tissue. But it may result in cartilage destruction without ossification at the avascular central area.

The fact that RUNX-2 insufficiency prevented both cartilage destruction and osteophyte formation without affecting physiologic skeletal conditions suggests that this molecule can clinically be a therapeutic target of these disorders, since RUNX-2 is known to be induced in human OA cartilage (46). Mutations in the *Runx2* gene cause cleidocranial dysplasia not only in mice, but also in humans (22,47,48). Although various types of the human *RUNX-2* gene, including chromosomal translocations, deletions, insertions, nonsense, missense, and splice-site mutations, have been reported to cause a wide spectrum of phenotypic variability, ranging from primary dental anomalies to all typical features plus osteoporosis, future studies on the susceptibility of OA in these patients will provide invaluable information on the possibility that RUNX-2 is a clinical target for this common joint disorder.

ACKNOWLEDGMENTS

REFERENCES

1. Doherty M. Risk factors for progression of knee osteoarthritis. Lancet 2001;358:775–6.
2. Poole AR, Howell DS. Etiopathies of osteoarthritis. In: Moskowitz RW, Howell DS, Altman RD, Buckwalter JA, Goldberg VM, editors. Osteoarthritis: Diagnosis and medical/surgical management. 3rd ed. Philadelphia: Saunders; 2001. p. 29–47.
3. Pond MJ, Nuki G. Experimentally-induced osteoarthritis in the dog. Ann Rheum Dis 1973;32:387–8.
4. Matyas JR, Ehlers PF, Huang D, Adams ME. The early molecular natural history of experimental osteoarthritis. I. Progressive discoordinate expression of aggrecan and type II procollagen messenger RNA in the articular cartilage of adult animals. Arthritis Rheum 1999;42:993–1002.
5. Le Graverand MP, Eggerer J, Vignon E, Otterness IG, Barclay L, Hart DA. Assessment of specific mRNA levels in cartilage regions in a lapine model of osteoarthritis. J Orthop Res 2002;20:535–44.
6. Matyas JR, Huang D, Chung M, Adams ME. Regional quantification of cartilage type II collagen and aggrecan messenger RNA in joints with early experimental osteoarthritis. Arthritis Rheum 2002;46:1536–43.
7. Bluteau G, Gouttenoire J, Conrozier T, Mathieu P, Vignon E, Richard M, et al. Differential gene expression analysis in a rabbit model of osteoarthritis induced by anterior cruciate ligament (ACL) section. Biorheology 2002;39:247–58.
8. Hayami T, Pickarski M, Wesolowski GA, McLane J, Bone A, Destefano J, et al. The role of subchondral bone remodeling in osteoarthritis: reduction of cartilage degeneration and prevention of osteophyte formation by alendronate in the rat anterior cruciate ligament transection model. Arthritis Rheum 2004;50:1193–206.
9. Lorenz H, Wenz W, Ivancic M, Steck E, Richter W. Early and stable upregulation of collagen type II, collagen type I and YKL40 expression levels in cartilage during early experimental osteoarthritis occurs independent of joint location and histological grading. Arthritis Res Ther 2005;7:R156–65.
10. Kamekura S, Hoshi K, Shimoaka T, Chung U, Chikuda H, Yamada T, et al. Osteoarthritis development in novel experimental mouse models induced by knee joint instability. Osteoarthritis Cartilage 2005;13:632–41.

11. Von der Mark K, Kirsch T, Nerlich A, Kuss A, Weseloh G, Gluckert K, et al. Type X collagen synthesis in human osteoarthritic cartilage: indication of chondrocyte hypertrophy. Arthritis Rheum 1992;35:806–11.

12. Boos N, Nerlich AG, Wiest I, von der Mark K, Ganz R, Aebi M. Immunohistochemical analysis of type-X-collagen expression in osteoarthritis of the hip joint. J Orthop Res 1999;17:495–502.

13. Ducy P, Zhang R, Geoffroy V, Ridall AL, Karsenty G. Osf2/Cbfa1: a transcriptional activator of osteoblast differentiation. Cell 1997;89:747–54.

14. Karsenty G, Wagner EF. Reaching a genetic and molecular understanding of skeletal development [review]. Dev Cell 2002;2: 389–406.

15. Inada M, Yasui T, Nomura S, Miyake S, Deguchi K, Himeno M, et al. Maturational disturbance of chondrocytes in Cbfa1-deficient mice. Dev Dyn 1999;214:279–90.

16. Kim IS, Otto F, Zabel B, Mundlos S. Regulation of chondrocyte differentiation by Cbfa1. Mech Dev 1999;80:159–70.

17. Enomoto H, Enomoto-Iwamoto M, Iwamoto M, Nomura S, Himeno M, Kitamura Y, et al. Cbfa1 is a positive regulatory factor in chondrocyte maturation. J Biol Chem 2000;275:8695–702.

18. Ueta C, Iwamoto M, Kanatani N, Yoshida C, Liu Y, Enomoto-Iwamoto M, et al. Skeletal malformations caused by overexpression of Cbfa1 or its dominant negative form in chondrocytes. J Cell Biol 2001;153:87–100.

19. Takeda S, Bonnamy JP, Owen MJ, Ducy P, Karsenty G. Continuous expression of Cbfa1 in nonhypertrophic chondrocytes uncovers its ability to induce hypertrophic chondrocyte differentiation and partially rescues Cbfa1-deficient mice. Genes Dev 2001;15:467–81.

20. Zheng Q, Zhou G, Morello R, Chen Y, Garcia-Rojas X, Lee B. Type X collagen gene regulation by Runx2 contributes directly to its hypertrophic chondrocyte-specific expression in vivo. J Cell Biol 2003;162:833–42.

21. Komori T, Yagi H, Nomura S, Yamaguchi A, Sasaki K, Deguchi K, et al. Targeted disruption of Cbfa1 results in a complete lack of bone formation owing to maturational arrest of osteoblasts. Cell 1997;89:755–64.

22. Otto F, Thornell AP, Crompton T, Denzel A, Gilmour KC, Rosewell IR, et al. Cbfa1, a candidate gene for cleidocranial dysplasia syndrome, is essential for osteoblast differentiation and bone development. Cell 1997;89:765–71.

23. Parfitt AM, Drezner MK, Glorieux FH, Kanis JA, Malluche H, Meunier PJ, et al. Bone histomorphometry: standardization of nomenclature, symbols, and units. J Bone Miner Res 1987;2:595–610.

24. Hoshi K, Komori T, Ozawa H. Morphological characterization of skeletal cells in Cbfa1-deficient mice. Bone 1999;25:639–51.

25. Xu L, Peng H, Wu D, Hu K, Goldring MB, Olsen BR, et al. Activation of the discoidin domain receptor 2 induces expression of matrix metalloproteinase 13 associated with osteoarthritis in mice. J Biol Chem 2005;280:548–55.

26. Jimenez MJ, Balbin M, Lopez JM, Alvarez J, Komori T, Lopez-Otin C. Collagenase 3 is a target of Cbfa1, a transcription factor of the runt gene family involved in bone formation. Mol Cell Biol 1999;19:4431–42.

27. Porte D, Tuckermann J, Becker M, Baumann B, Teurich S, Higgins T, et al. Both AP-1 and Cbfa1-like factors are required for the induction of interstitial collagenase by parathyroid hormone. Oncogene 1999;18:667–78.

28. Neuhold LA, Killar L, Zhao W, Sung ML, Warner L, Kulik J, et al. Postnatal expression in hyaline cartilage of constitutively active human collagenase-3 (MMP-13) induces osteoarthritis in mice. J Clin Invest 2001;107:35–44.

29. Pullig O, Weseloh G, Gauer S, Swoboda B. Osteopontin is expressed by adult human osteoarthritic chondrocytes: protein and mRNA analysis of normal and osteoarthritic cartilage. Matrix Biol 2000;19:245–55.

30. Pullig O, Weseloh G, Ronneberger D, Kakonen S, Swoboda B. Chondrocyte differentiation in human osteoarthritis: expression of osteocalcin in normal and osteoarthritic cartilage and bone. Calcif Tissue Int 2000;67:230–40.

31. Pfander D, Swoboda B, Kirsch T. Expression of early and late differentiation markers (proliferating cell nuclear antigen, syndecan-3, annexin VI, and alkaline phosphatase) by human osteoarthritic chondrocytes. Am J Pathol 2001;159:1777–83.

32. Billinghurst RC, Dahlberg L, Ionescu M, Reiner A, Bourne R, Rorabeck C, et al. Enhanced cleavage of type II collagen by collagenases in osteoarthritic articular cartilage. J Clin Invest 1997;99:1534–45.

33. Vincenti MP, Brinckerhoff CE. Transcriptional regulation of collagenase (MMP-1, MMP-13) genes in arthritis: integration of complex signaling pathways for the recruitment of gene-specific transcription factors [review]. Arthritis Res 2002;4:157–64.

34. Manabe N, Oda H, Nakamura K, Kuga Y, Uchida S, Kawaguchi H. Involvement of fibroblast growth factor-2 in joint destruction of rheumatoid arthritis patients. Rheumatology (Oxford) 1999;38: 714–20.

35. Clements KM, Price JS, Chambers MG, Visco DM, Poole AR, Mason RM. Gene deletion of either interleukin-1β, interleukin-1β–converting enzyme, inducible nitric oxide synthase, or stromelysin 1 accelerates the development of knee osteoarthritis in mice after surgical transection of the medial collateral ligament and partial medial meniscectomy. Arthritis Rheum 2003;48:3452–63.

36. D'Angelo M, Yan Z, Nooreyazdan M, Pacifici M, Sarment DS, Billings PC, et al. MMP-13 is induced during chondrocyte hypertrophy. J Cell Biochem 2000;77:678–93.

37. Jimenez MJ, Balbin M, Alvarez J, Komori T, Bianco P, Holmbeck K, et al. A regulatory cascade involving retinoic acid, Cbfa1, and matrix metalloproteinases is coupled to the development of a process of perichondrial invasion and osteogenic differentiation during bone formation. J Cell Biol 2001;155:1333–44.

38. Ziros PG, Gil AP, Georgakopoulos T, Habeos I, Kletsas D, Basdra EK, et al. The bone-specific transcriptional regulator Cbfa1 is a target of mechanical signals in osteoblastic cells. J Biol Chem 2002;277:23934–41.

39. Costessi A, Pines A, D'Andrea P, Romanello M, Damante G, Cesaratto L, et al. Extracellular nucleotides activate Runx2 in the osteoblast-like HOBIT cell line: a possible molecular link between mechanical stress and osteoblasts' response. Bone 2005;36:418–32.

40. Wong M, Siegrist M, Goodwin K. Cyclic tensile strain and cyclic hydrostatic pressure differentially regulate expression of hypertrophic markers in primary chondrocytes. Bone 2003;33:685–93.

41. Shimoaka T, Kamekura S, Chikuda H, Hoshi K, Chung UI, Akune T, et al. Impairment of bone healing by insulin receptor substrate-1 deficiency. J Biol Chem 2004;279:15314–22.

42. Radin EL, Rose RM. Role of subchondral bone in the initiation and progression of cartilage damage. Clin Orthop Relat Res 1986;213:34–40.

43. Burr DB. The importance of subchondral bone in osteoarthrosis [review]. Curr Opin Rheumatol 1998;10:256–62.

44. Glasson SS, Askew R, Sheppard B, Carito B, Blanchet T, Ma HL, et al. Deletion of active ADAMTS5 prevents cartilage degradation in a murine model of osteoarthritis. Nature 2005;434:644–8.

45. Stanton H, Rogerson FM, East CJ, Golub SB, Lawlor KE, Meeker CT, et al. ADAMTS5 is the major aggrecanase in mouse cartilage in vivo and in vitro. Nature 2005;434:648–52.

46. Wang X, Manner PA, Horner A, Shum L, Tuan RS, Nuckolls GH. Regulation of MMP-13 expression by RUNX2 and FGF2 in osteoarthritic cartilage. Osteoarthritis Cartilage 2004;12:963–73.

47. Mundlos S, Otto F, Mundlos C, Mulliken JB, Aylsworth AS, Albright S, et al. Mutations involving the transcription factor CBFA1 cause cleidocranial dysplasia. Cell 1997;89:773–9.

48. Otto F, Kanegane H, Mundlos S. Mutations in the RUNX2 gene in patients with cleidocranial dysplasia [review]. Hum Mutat 2002;19:209–16.

Short communication

Extracorporeal shockwaves induce the expression of ATF3 and GAP-43 in rat dorsal root ganglion neurons

Ryo Murata [a,*], Seiji Ohtori [a], Nobuyasu Ochiai [a], Norimasa Takahashi [a], Takashi Saisu [b], Hideshige Moriya [a], Kazuhisa Takahashi [a], Yuichi Wada [c]

[a] Department of Orthopaedic Surgery, Graduate School of Medicine, Chiba University, Chiba, Japan
[b] Division of Orthopaedic Surgery, Chiba Children's Hospital, Chiba, Japan
[c] Department of Orthopaedic Surgery, Teikyo University Ichihara Hospital, Ichihara, Chiba, Japan

Abstract

Although extracorporeal shockwave has been applied in the treatment of various diseases, the biological basis for its analgesic effect remains unclear. Therefore, we investigated the dorsal root ganglion neurons of rats following shockwave exposure to the footpad to elucidate its effect on the peripheral nervous system. We used activating transcription factor 3 (ATF3) and growth-associated phosphoprotein (GAP-43) as markers for nerve injury and axonal regeneration, respectively. The average number of neurons immunoreactive for ATF3 increased significantly in the treated rats at all experimental time points, with 78.3% of those neurons also exhibiting immunoreactivity for GAP-43. Shockwave exposure induced injury of the sensory nerve fibers within the exposed area. This phenomenon may be linked to the desensitization of the exposure area, not the cause of pain, considering clinical research with a particular absence of painful adverse effect. Subsequent active axonal regeneration may account for the reinnervation of exposed area and the amelioration of the desensitization.
© 2006 Elsevier B.V. All rights reserved.

Keywords: Shockwave; Analgesic effect; Nerve fiber; Injury; Regeneration

Extracorporeal shockwave therapy (ESW) has become better known as an approach for the management of various painful orthopedic disorders (Gerdesmeyer et al., 2003; Rompe et al., 1996, 2004). Despite the increasing recognition of ESW, only a few studies have investigated its biological effects on the nervous system and the mechanism of its analgesic effect (Maier et al., 2003; Haake et al., 2002).

We have previously shown that ESW of the rat footpad caused degeneration and reinnervation of sensory nerve fibers innervating the skin (Ohtori et al., 2001). ESW also caused a decrease in immunoreactivity for calcitonin gene-related peptide (CGRP) in dorsal root ganglion (DRG) neurons (Takahashi et al., 2003). The biological effects of ESW in other components of the sensory

nervous system such as the DRG and spinal cord warrant further investigation.

Activating transcription factor 3 (ATF3) is specifically induced in DRG neurons and the spinal cord neurons after nerve injury. ATF3 is a member of the ATF/CREB family of transcription factors and its expression is induced in a variety of tissues exposed to stress (Hai et al., 1999). Although its function has not been clearly elucidated, ATF3 is widely regarded as a specific neuronal marker of nerve injury (Hai et al., 1999; Tsujino et al., 2000). On the other hand, growth-associated phosphoprotein (GAP-43) has emerged as one of the most useful markers of axonal regeneration (Skene and Willard, 1981), and is expressed at particularly high levels in developing neurons and elongating axonal growth cones (Jacobson et al., 1986). Nerve injury leads to increased synthesis of GAP-43 in adult neurons (Coggins and Zwiers, 1991). If ESW to the skin were to have effects on DRG neurons, observed changes in expression of these markers

may provide insight into the biological effects of ESW on the peripheral nervous system. With this in mind, we investigated changes in ATF3 and GAP-43 expression profiles in DRG neurons following ESW of the rat footpad.

Experiments were conducted in accordance with the guidelines for animal experimentation of the Ethics Review Committee of Chiba University. Twenty-eight male Sprague–Dawley rats weighing 250–300 g were used. Rats receiving ESW (the ESW group) were generally anaesthetized with an intraperitoneal injection of 40 mg/kg sodium pentobarbital before shockwave exposure. Two-thousand shockwave pulses at an energy flux density of 0.08 mJ/mm^2 and a frequency of 4 Hz generated by a lithotripter (Dornier Med. Tech.; Epos®) were applied to the skin of footpads corresponding to the L4 and L5 dermatomes as previously described (Takahashi et al., 1994).

On 1, 2, 4, 7, 14 and 28 days after the shockwave exposure, four rats each in the ESW group were anesthetized with 40 mg/kg sodium pentobarbital and perfused transcardially with 0.9% saline, followed by 500 ml of 4% paraformaldehyde in a phosphate buffer (0.1 M. pH 7.4). After fixation, the L4 and L5 DRG of the rats were collected bilaterally. The other four rats received no shockwaves and were used as controls; the bilateral L4 and L5 DRG were collected in the same manner as for the ESW group. After storage in 0.01 M phosphate-buffered saline (PBS) containing 20% sucrose at 4 °C for 20 h, the specimens were serially sectioned on a cryostat at 20 μm intervals.

The sections were treated in blocking solution (0.01 M PBS containing 0.3% Triton X-100 and 1% normal goat serum) at room temperature for 90 min. They were then incubated at 4 °C for 20 h in rabbit antibody for ATF3 (1:200; Santa Cruz Biotechnology, Santa Cruz, CA) and mouse antibody for GAP-43 (1:1000; Sigma, St. Louis, MO) diluted in blocking solution. After they were washed three times in PBS, the sections were incubated with secondary antibodies (Alexa 594-labeled anti-mouse antibodies [1:250; Molecular Probes, Eugene, OR] and Alexa 488-labeled anti-rabbit antibodies [1:250; Molecular Probes,

Eugene, OR]). The sections were then examined using a fluorescence microscope.

To quantify immunoreactivity, we counted the total number of ATF3 immunoreactive neurons (ATF3-IR neurons) and both ATF3 and GAP-43 immunoreactive neurons (ATF3/GAP-43 dual-IR neurons) in profile in every third section across each harvested DRG. Moreover, immunoreactive neurons were divided into two groups according to their cell diameter: small (<30 μm) and large (>30 μm) neurons, as determined by a graticule scale. All data was analysed by a blinded observer.

Statistical significance of differences between the ESW group and the control was determined by Tukey's test for equal sample variance with a confidence level greater than 95% ($P<0.05$).

Scattered ATF3-IR neurons were observed in DRG of the ESW group (Fig. 1A). In contrast, ATF3-IR neurons were rarely detected in DRG of the control group (Fig. 1B). Many aspects of ATF3-IR neurons seemed to also be immunoreactive for GAP-43 (Fig. 1C).

The average number of ATF3-IR neurons and ATF3/GAP-43 dual-IR neurons was significantly larger in the ESW group than in the control group at all time points (Fig. 2). The number of neither the ATF3-IR neurons nor the ATF3/GAP-43 dual-IR neurons showed a significant time dependence during the period studied (Fig. 2).

In total of all time points, 1969 immunoreactive neurons were observed in the ESW group (Table 1). The ratios of small neurons and large neurons to the total ATF3-IR neurons were 22.5% (444/1969) and 77.5% (1525/1969), respectively; 78.3% (1542/1969) of ATF3-IR neurons were also immunoreactive for GAP-43. Among the ATF3-IR neurons, 44.3% (197/444) of small neurons and 88.1% (1345/1525) of large neurons were also immunoreactive for GAP-43. The ratios of small and large ATF3/GAP-43 dual-IR neurons to the total ATF3/GAP-43 dual-IR neurons were 12.8% (197/1542) and 87.2% (1345/1542), respectively. The neurons immunoreactive for GAP-43 alone seemed to be in the majority, although we had not counted them precisely.
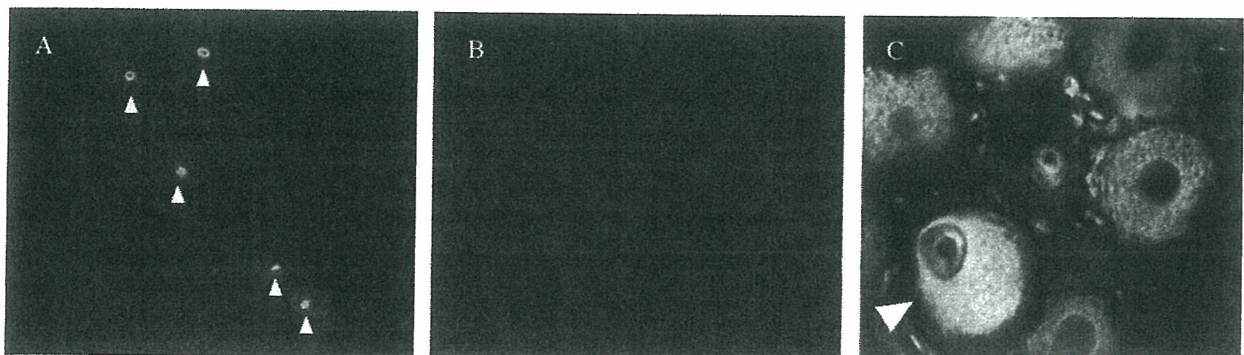

Fig. 1. Fluorescence microscopic images of dorsal root ganglion (DRG). A (×100): A section from L5 DRG in the ESW group 4 days after application of ESW. Several neurons with well-stained nuclei immunoreactive for ATF3 (arrowheads) are observed. B (×100): A section from L5 DRG in the control group. ATF3-IR neurons could not be detected in this section. C (×400): Merged images from L5 DRG in the ESWT group of 2 days after ESWT. An ATF3/GAP-43 dual-IR neuron with a well-stained nucleus and cytoplasm (arrowhead) is shown.

Total number of the profile of immunoreactive neurons
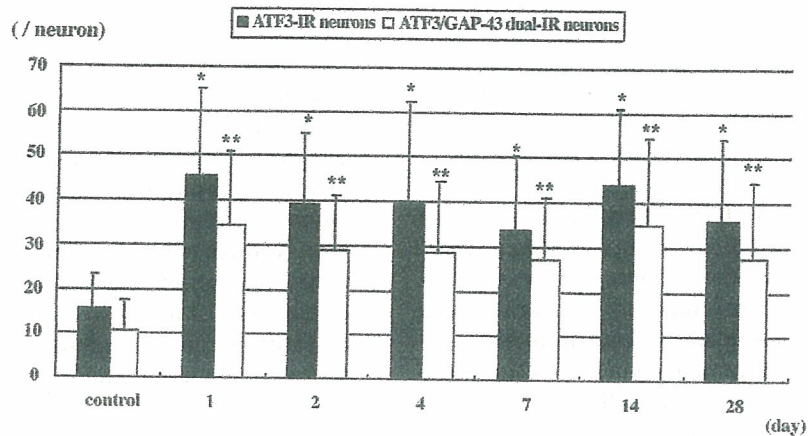

Fig. 2. Total profile of immunoreactive neurons. ATF3-IR neurons: neurons immunoreactive for ATF3. ATF3/GAP-43 dual-IR neurons: neurons immunoreactive for both ATF3 and GAP-43. This graph illustrates the total number of ATF3-IR neuron profiles (black column) and ATF3/GAP-43 dual-IR neuron profiles (white column). The symbols (*, **) indicate the significance of the difference of the data by Tukey's test compared to controls ($n=4$, $P<0.05$). All data were shown as mean values+S.D.

In this study, we showed that ESW to the rat footpad caused nerve injury as indicated by increased numbers of ATF3-IR neurons, and axonal regeneration by those neurons double labeled for ATF3 and GAP-43 immunoreactivity.

ATF3 is involved in the stress response (Hai et al., 1999). ATF3 is also known as a transcriptional repressor and is implicated in the cell death of some non-neuronal cells (Chen et al., 1994; Mashima et al., 2001; Nawa et al., 2002; Zhang et al., 2001). In the nervous system, ATF3 has been designated as a marker for nerve injury because of its specific expression in response to nerve injury (Tsujino et al., 2000; Obata et al., 2003). The rat model for nerve damage utilizing resection of the sciatic nerve has produced ATF3 immunoreactivity in a majority of DRG neurons (Tsujino et al., 2000; Obata et al., 2003), whereas our model showed fewer ATF3-IR neurons. Although the functional consequence of ATF3 in nerve injury has not been elucidated, this difference of ATF3 immunoreactivity may be related to a

difference in the number of affected nerve fibers. The lithotripter we used generated focused shockwaves with an exposure area of approximately $5\times5\times26$ mm. The small number of nerve fibers within this area of narrow exposure might only be expected to produce weak ATF3 expression on the corresponding DRG, which is consistent with our observations.

In general, there is no simple correlation between epidermal innervation and sensory functions such as nociception (Lindenlaub and Sommer, 2002). Spinal and peripheral nerve injury often accounts for neuropathic or phantom pain (Chung et al., 1993; Devor et al., 1994; Ma and Bisby, 2000; McLachlan et al., 1993; O'Halloran and Perl, 1997; Verdu and Navarro, 1997). Previous clinical research focusing on ESW has shown significant pain relief and only few side effects, with a particular absence of problems such as neuropathic pain (Gerdesmeyer et al., 2003; Rompe et al., 1996, 2004). Thus, the increase of ATF3-IR DRG neuron number induced by ESW may be linked to the desensitization of the exposure area, not the cause of the neuropathic pain.

The significant increase in the number of ATF3-IR neurons after exposure was sustained for at least 28 days (Fig. 2). This observation, however, does not confirm a persistent desensitization of the exposed area. The presence of ATF3/GAP-43 dual-IR neurons, which account for 78.3% (1542/1969) of ATF3-IR neurons, may indicate the regeneration of injured nerve fibers (Table 1). GAP-43 is a 24 kDa neuronal-specific phosphoprotein, which is implicated in axogenesis and synaptogenesis during regeneration of the nervous system (Karns et al., 1987; Bomze et al., 2001). The expression of GAP-43 mRNA is induced early in the cell soma and proximal axon after axotomy (Hoffman, 1989; Verge et al., 1990; Tetzlaff et al., 1991). In the current study,

Table 1

Size distribution of immunopositive neurons of the ESW group

	ATF3-IR neurons		
	ATF3/GAP-43 dual-IR neurons		Total
Small (<30 μm)	197		444
Large (>30 μm)	1345		1525
Total	1542		1969

This table shows the total number of immunopositive neurons of the ESW group. All data indicate combined number of all time points. Immunoreactive neurons were classified according to cell diameter measured by graticule scale as small (<30 μm) and large (>30 μm). All values were shown as the number of neurons in each category.

ATF3-IR neurons: neurons immunoreactive for ATF3.

ATF3/GAP-43 dual-IR neurons: neurons immunoreactive for both ATF3 and GAP-43.

GAP-43 immunoreactivity was represented by exclusively well-stained cytoplasm, which had supported this finding. The regeneration phase of injured nerve fibers, indicated by the expression of ATF3/GAP-43 dual-IR neurons, began within a day of the ESW application. We found that most of the nerve fibers degenerated by ESW reinnervated the exposure area, penetrating the basal lamina of the epithelium within 14 days of the ESW application (Ohtori et al., 2001). The time difference in these findings suggests that actual elongation of damaged nerve fibers to the skin may require longer than GAP-43 expression in neuron after the ESW application. This rapid reinnervation of the exposed area could contribute to the amelioration of desensitization.

With regard to the size distribution of ATF3-IR neurons, 22.5% (444/1969) were classified as small neurons (Table 1). The sensory nerve fibers originating from small neurons are mainly of small diameter, suggesting their involvement in nociception, temperature perception and autonomic effects. Adrenergic sprouting induced after nerve lesions in nociceptive C-fibers (Sato and Perl, 1991) and DRG (McLachlan et al., 1993; Ramer et al., 1998) is thought to result from states of neuropathic pain. Thus, the injury of nerve fibers originating from small ATF3-IR neurons may be associated with the alleviation of pain.

However, 44.3% (197/444) of ATF3-IR small neurons also showed immunoreactivity for GAP-43 (Table 1), possibly indicating axonal regeneration of the injured small-diameter fibers. This proportion is much higher than the previously reported proportion of approximately 3% in normal DRG immunoreactive neurons in rats (Gonzalez-Hernandez and Rustioni, 1999). The up-regulation of ATF3/GAP-43 dual-IR small neurons most likely represented active axonal regeneration of the injured nerve fibers, which may indicate the recurrence of pain.

Moreover, 77.5% (1525/1969) of ATF3-IR neurons were classified as large neurons (Table 1). Most ATF3-IR DRG neurons had been observed in the rat sciatic nerve resection model are of medium to large diameter (Obata et al., 2003), indicating that large-diameter fibers such as Aα or Aβ fibers account for most of the injury, and small-diameter fibers such as Aδ or C-fibers were relatively uninjured. Although a difference in vulnerability between these fibers has not been established (Fröhling et al., 1998), large-diameter fibers are thought to be more sensitive to ESW than small-diameter fibers. These observations may help explain the analgesic effect of ESW, since large-diameter fibers play a crucial role in painful conditions such as allodynia (McLachlan et al., 1993).

This study has several potential limitations. We have counted the profile of immunoreactive neurons, but could not estimate the actual number of immunoreactive neurons (Coggeshall and Lekan, 1996). We examined DRG neurons immunohistochemically, but we did not directly evaluate any pain associated with the cellular effects observed. The analgesic effect of ESW may not be proven by physiological examination employing normal animal models. Study of the analgesic effects of ESW, especially physiological effects, should perhaps utilize pathological models of pain. The relevance of cellular ATF3 or GAP-43 levels with regard to the analgesic effect in clinical subjects has not been elucidated.

Nevertheless, this study shows that ESW induced peripheral nerve injury and regeneration of the nerve fibers originating from DRG neurons in rats, and that the nerve injury may contribute to the desensitization of the exposed area. The regeneration of injured nerve fibers may occur immediately after exposure and account for the reinnervation of the exposed area. These observations provide a partial explanation for the analgesic effects of ESW and may contribute to the elucidation of pain recurrence observed in clinical subjects.

References

Bomze, H.M., Bulsara, K.R., Iskandar, B.J., Caroni, P., Skene, J.H., 2001. Spinal axon regeneration evoked by replacing tow growth cone proteins in adult neurons. Nat. Neurosci. 4, 38–43.

Chen, B.P., Liang, G., Whelan, J., Hai, T., 1994. ATF3 and ATF3 delta Zip. Transcriptional repression versus activation by alternatively spliced isoforms. J. Biol. Chem. 269, 15819–15826.

Chung, K., Kim, H.J., Na, H.S., Park, M.J., Chung, J.M., 1993. Abnormalities of sympathetic innervation in the area of an injured peripheral nerve in a rat model of neuropathic pain. Neurosci. Lett. 162, 85–88.

Coggeshall, R.E., Lekan, H.A., 1996. Methods for determining numbers of cells and synapses: a case for more uniform standards of review. J. Comp. Neurol. 364, 6–15.

Coggins, P.J., Zwiers, H., 1991. B-50 (GAP-43): biochemistry and functional neurochemistry of a neuron-specific phosphoprotein. J. Neurochem. 56, 1095–1106.

Devor, M., Janig, W., Michaelis, M., 1994. Modulation of activity in dorsal root ganglion neurons by sympathetic activation in nerve-injured rats. J. Neurophysiol. 71, 38–47.

Fröhling, M.A., Schlote, W., Wolburg-Buchholz, K., 1998. Nonselective nerve fibre damage in peripheral nerves after experimental thermocoagulation. Acta Neurochir. 140, 1297–1302.

Gerdesmeyer, L., Wagenpfeil, S., Haake, M., Maier, M., Loew, M., Wortler, K., Lampe, R., Seil, R., Handle, G., Gassel, S., Rompe, J.D., 2003. Extracorporeal shock wave therapy for the treatment of chronic calcifying tendonitis of the rotator cuff: a randomized controlled trial. JAMA 290, 2573–2580.

Gonzalez-Hernandez, T., Rustioni, A., 1999. Nitric oxide synthase and growth-associated protein are coexpressed in primary sensory neurons after peripheral injury. J. Comp. Neurol. 404, 64–74.

Haake, M., Thon, A., Bette, M., 2002. Unchanged c-Fos expression after extracorporeal shock wave therapy: an experimental investigation in rats. Arch. Orthop. Trauma Surg. 122, 518–521.

Hai, T., Wolfgang, C.D., Marsee, D.K., Allen, A.E., Sivaprasad, U., 1999. ATF3 and stress responses. Gene Expression 7, 321–335.

Hoffman, P.N., 1989. Expression of GAP-43, a rapidly transported growth-associated protein, and class 2 beta tubulin, a slowly transported cytoskeletal protein, are coordinated in regenerating neurons. J. Neurosci. 9, 893–897.

Jacobson, R.D., Virag, I., Skene, J.H., 1986. A protein associated with axon growth, GAP-43, is widely distributed and developmentally regulated in rat CNS. J. Neurosci. 6, 1843–1855.

Karns, L.R., Ng, S.C., Freeman, J.A., Fishman, M.C., 1987. Cloning of complementary DNA for GAP-43, a neuronal growth-related protein. Science 236, 597–600.

Lindenlaub, T., Sommer, C., 2002. Epidermal innervation density after partial sciatic nerve lesion and pain-related behavior in the rat. Acta Neuropathol. 104, 137–143.

Ma, W., Bisby, M.A., 2000. Calcitonin gene-related peptide, substance P and protein gene product 9.5 immunoreactive axonal fibers in the rat footpad skin following partial sciatic nerve injuries. J. Neurocytol. 29, 249–262.

Maier, M., Averbeck, B., Milz, S., Refior, H.J., Schmitz, C., 2003. Substance P and prostaglandin E2 release after shock wave application to the rabbit femur. Clin. Orthop. Relat. Res. 406, 237–245.

Mashima, T., Udagawa, S., Tsuruo, T., 2001. Involvement of transcriptional repressor ATF3 in acceleration of caspase protease activation during DNA damaging agent-induced apoptosis. J. Cell. Physiol. 188, 352–358.

McLachlan, E.M., Janig, W., Devor, M., Michaelis, M., 1993. Peripheral nerve injury triggers noradrenergic sprouting within dorsal root ganglia. Nature 363, 543–546.

Nawa, T., Nawa, M.T., Adachi, M.T., Uchimura, I., Shimokawa, R., Fujisawa, K., Tanaka, A., Numano, F., Kitajima, S., 2002. Expression of transcriptional repressor ATF3/LRF1 in human atherosclerosis: colocalization and possible involvement in cell death of vascular endothelial cells. Atherosclerosis 161, 281–291.

Obata, K., Yamanaka, H., Fukuoka, T., Yi, D., Tokunaga, A., Hashimoto, N., Yoshinaga, H., Noguchi, K., 2003. Contribution of injured and uninjured dorsal root ganglion neurons to pain behavior and the changes in gene expression following chronic constriction model of the sciatic nerve in rats. Pain 101, 65–77.

O'Halloran, K.D., Perl, E.R., 1997. Effects of partial nerve injury on the responses of C-fiber polymodal nociceptors to adrenergic agonists. Brain Res. 759, 233–240.

Ohtori, S., Inoue, G., Mannoji, C., Saisu, T., Takahashi, K., Mitsuhashi, S., Wada, Y., Takahashi, K., Yamagata, M., Moriya, H., 2001. Shock wave application to rat skin induces degeneration and reinnervation of sensory nerve fibers. Neurosci. Lett. 315, 57–60.

Ramer, M.S., Murphy, P.G., Richardson, P.M., Bisby, M.A., 1998. Spinal nerve lesion-induced mechanoallodynia and adrenergic sprouting in sensory ganglia are attenuated in interleukin-6 knockout mice. Pain 78, 115–121.

Rompe, J.D., Hopf, C., Küllmer, K., Heine, J., Bürger, R., 1996. Analgesic effect of extracorporeal shock-wave therapy on chronic tennis elbow. J. Bone Jt. Surg. 78-B, 233–237.

Rompe, J.D., Decking, J., Schöellner, C., Theis, C., 2004. Repetitive low-energy shock wave treatment for chronic lateral epicondylitis in tennis players. Am. J. Sports Med. 32, 734–743.

Sato, J., Perl, E.R., 1991. Adrenergic excitation of cutaneous pain receptors induced by peripheral nerve injury. Science 251, 1608–1610.

Skene, J.H., Willard, M., 1981. Axonally transported proteins associated with axon growth in rabbit central and peripheral nervous system. J. Cell Biol. 89, 96–103.

Takahashi, Y., Nakajima, Y., Sakamoto, T., 1994. Dermatome mapping in the rat hindlimb by electrical stimulation of the spinal nerves. Neurosci. Lett. 168, 85–88.

Takahashi, N., Wada, Y., Ohtori, S., Saisu, T., Moriya, H., 2003. Application of shock wave to rat skin decreases calcitonin gene-related peptide immunoreactivity in dorsal root ganglion neurons. Auton. Neurosci. 107, 91–94.

Tetzlaff, W., Alexander, S.W., Miller, F.D., Bisby, M.A., 1991. Response of facial and rubrospinal neurons to axotomy: changes in mRNA expression for cytoskeletal proteins and GAP-43. J. Neurosci. 11, 2528–2544.

Tsujino, H., Kondo, E., Fukuoka, T., Dai, Y., Tokunaga, A., Miki, K., Yonenobu, K., Ochi, T., Noguchi, K., 2000. Activating transcription factor 3 (ATF3) induction by axotomy in sensory and motoneurons: a novel neuronal marker of nerve injury. Mol. Cell. Neurosci. 15, 170–182.

Verdu, E., Navarro, X., 1997. Comparison of immunohistochemical and functional reinnervation of skin and muscle after peripheral nerve injury. Exp. Neurol. 146, 187–198.

Verge, V.M., Tetzlaff, W., Richardson, P.M., Bisby, M.A., 1990. Correlation between GAP43 and nerve growth factor receptors in rat sensory neurons. J. Neurosci. 10, 926–934.

Zhang, C., Kawauchi, J., Adachi, M.T., Hashimoto, Y., Oshiro, S., Aso, T., Kitajima, S., 2001. Activation of JNK and transcriptional repressor ATF3/LRF1 through the IRE1/TRAF2 pathway is implicated in human vascular endothelial cell death by homocysteine. Biochem. Biophys. Res. Commun. 289, 718–724.

ELSEVIER

Mechanical and histological evaluation of a PMMA-based bone cement modified with γ-methacryloxypropyltrimethoxysilane and calcium acetate

Tadashi Tsukeoka[a,*], Masahiko Suzuki[a,*], Chikara Ohtsuki[b], Atsushi Sugino[b,c],
Yoshikazu Tsuneizumi[a], Jin Miyagi[a], Kouichi Kuramoto[c], Hideshige Moriya[a]

[a]*Department of Orthopaedic Surgery, Graduate School of Medicine, Chiba University, 1-8-1 Inohana, Chuo-ku, Chiba 260-8677, Japan*
[b]*Graduate School of Materials Science, Nara Institute of Science and Technology, 8916-5 Takayama-cho, Ikoma-shi, Nara 630-0192, Japan*
[c]*Nakashima Medical Division, Nakashima Propeller Co. Ltd., 688-1 Jodo-Kitagata, Okayama 700-8691, Japan*

Abstract

Polymethylmethacrylate (PMMA) bone cement is widely used for prosthetic fixation in orthopaedic surgery; however, the interface between bone and cement is a weak zone. We developed a bioactive PMMA cement through modification with γ-methacryloxypropyl-trimethoxysilane (MPS) and calcium acetate. The purpose of this study was to compare the handling, mechanical and histological properties of the modified bone cement with those of the conventional cement. The modified specimens exhibited higher bonding strength between bone and implant. Histological observation and micro-focus X-ray computed tomogram (micro-CT) images showed that the modified cement exhibited osteoconduction, which the conventional PMMA bone cement lacked. The modification was found to be effective in enabling osteoconduction with PMMA bone cement, thus providing stable fixation for a long period after implantation.
© 2006 Elsevier Ltd. All rights reserved.

Keywords: Bioactivity; Bone cement; Mechanical property; In vitro test; In vivo test

1. Introduction

Polymethylmethacrylate (PMMA) bone cement has been widely used for prosthetic fixation in orthopaedic surgery. Among the zones that include prosthesis–bone cement–bone, the interface between bone and PMMA bone cement is known as one of the weak-link zones, because conventional PMMA bone cement is unable to bond to living bone [1]. One may expect that providing PMMA bone cement with bone-bonding ability, the so-called bioactivity, would solve the problem of fixation between living bone and PMMA bone cement.

Previously, powders of bioactive ceramics such as sintered hydroxyapatite and glass–ceramic A-W were added to PMMA bone cement [2,3] to fabricate bioactive bone cement. More than 60 wt% of bioactive ceramic powder should be included in PMMA powders to satisfy the osteoconductive properties after setting. Inadequate amounts of ceramic powder in the cement might leave less area of the bioactive fillers to react with the surrounding body fluid, on exposure to the body environment. Moreover, addition of excess amounts of ceramic power to the PMMA cement might adversely affect the mechanical and handling properties [4]. Modification of the methylmethacrylate (MMA) liquid is one of the possible methods to reduce the fraction of additives to the bioactive ceramic fillers, since the surface of the set cement should react with the surrounding body fluid. Previous studies on bone-bonding mechanisms of bioactive ceramics revealed that the essential requirement for an artificial material to bond to bone is the formation of an apatite layer on its surface after implantation in bony defects [5,6]. The apatite formation is triggered by the release of calcium ions (Ca^{2+}) from the surface of the bioactive materials, and by

*Corresponding author. Tel.: +81 43 222 7171; fax: +81 43 226 2116.

E-mail addresses: mdddd940@ybb.ne.jp (T. Tsukeoka),
masahiko@med.m.chiba-u.ac.jp (M. Suzuki).

the inductive effects of silanol (Si–OH) group on heterogeneous nucleation of the apatite layer under body environment [7]. Based on these mechanisms, we have proposed the development of a bioactive PMMA cement, modified with alkoxysilane compounds, which provides Si–OH groups, as well as calcium salts, which release Ca^{2+}. In our previous evaluation of several PMMA bone cements modified with alkoxysilane and calcium salts, the modification with 20 mass% of γ-methacryloxypropyltrimethoxysilane (MPS) and calcium acetate resulted in bioactive PMMA bone cement [8,9]. This modified PMMA was intended for prosthetic fixation. It should be noted that the quantity of additives in our modified cement was much lower than that in the previously reported method, i.e., 70 mass%. With this lower content of additives, our modified cement may exhibit better handling characteristics and mechanical properties. Few studies have reported the use of MPS in vivo, and hence toxicity of MPS in living tissue remains uncertain. In this study, the modified PMMA cement with MPS and calcium acetate was further evaluated to determine its handling characteristics, mechanical properties and behavior in a simulated body fluid (SBF). The possible problems with the application of the modified cement are discussed by comparing with the characters of commercially available conventional PMMA bone cement.

2. Materials and methods

2.1. Preparation of the modified PMMA bone cement

Modified PMMA bone cement was prepared according to a previous report [10]. The raw materials used for the preparation and the composition of modified PMMA bone cement are listed in Table 1. Calcium acetate monohydrate ($Ca(CH_3COO)_2 \cdot H_2O$) was pulverized to a size of less than 44 μm and calcined at 220 °C for 2 h in order to remove the water in the compounds. The PMMA powder that had an approximate molecular weight of 100,000 and average particle size of 14 μm was purchased from Sekisui Plastics Co. Ltd. The PMMA powder was mixed with heat-treated calcium acetate, as well as barium sulfate ($BaSO_4$) as radio-opaque filler and benzoyl peroxide (BPO) as polymerization initiator without further purification. The liquid components were prepared by mixing the chemical reagents, namely MMA, γ-MPS and N,N-dimethyl-p-toluidine (NDT) as polymerization accelerator. The paste was prepared by mixing the powder with the liquid at a powder-to-liquid

(P/L) mass ratio of 2:1 under ambient conditions at room temperature. Zimmer® dough-type radio-opaque cement (Zimmer, Warsaw, IN, USA) was used as a reference of the commercialized conventional PMMA bone cement.

2.2. Measurement of the setting time and temperature during polymerization

Setting behavior of the mixed pastes was evaluated according to ISO5833 [11]. The paste, which was a mixture of the powder and liquid, was packed into a cylindrical mold (60 mm in diameter, 6 mm in height). The temperature measurement probe (CM-16635, HFT-40, Anritsu Meter Co. Ltd., Tokyo, Japan) was then installed into the center of the mold to measure the curing temperature every 20 s, until the temperature begins to fall. The maximum temperature, T_{max}, during polymerization was determined to plot the recorded temperature against time. The setting time was calculated using the following:

$$T = (T_{max} + T_{amb})/2, \tag{1}$$

where T was the setting temperature and T_{amb} was the recorded ambient temperature. The setting time was determined from the beginning of the mixing until the T value reaches. These experiments were carried out three times and the average and standard deviation calculated.

2.3. Compressive strength

For the compressive strength measurement, the cements were molded to the cylindrical specimens 6 mm in diameter and 12 mm in length. After curing, the cement was kept for 24 h in the air at room temperature. Moreover, molded specimens were exposed to SBF at 36.5 °C at a solution/surface area ratio = 0.1 ml/mm² before it was completely cured, and kept for 7 days. SBF proposed by Kokubo and his colleagues [12] was used in this study. Ion concentrations of SBF are Na^+ 142.0, K^+ 5.0, Mg^{2+} 1.5, Ca^{2+} 2.5, Cl^- 147.8, HCO_3^- 4.2, HPO_4^{2-} 1.0 and SO_4^{2-} 0.5 mM ($= mol/m^3$). The compressive load was applied at cross-head speed of 20 mm/min using the material testing machine (EHF-F01, Shimadzu Co., Kyoto, Japan) until fracture occurred. The compressive strength was calculated from compressive load and geometric area of the specimens. The average compressive strength and standard deviation were calculated.

2.4. Behavior of the specimen in SBF

Surface morphological changes and apatite formation on the cements after exposure to SBF were observed for the cements molded into rectangular shapes of $10 \times 15 \times 1$ mm. Before the molded cements were completely cured, the specimens were immersed in 35 ml of SBF at 36.5 °C. After 1, 3 and 7 days, the specimens were removed from the solution, and gently washed with distilled water. Surface changes of the specimens were characterized by thin-film X-ray diffraction (TF-XRD, RINT2500, Rigaku Co., Tokyo, Japan), field emission scanning electron microscopy

Table 1
Composition of the examined cement

Components	Mass ratio	Note
Powder		
PMMA	0.680	Sekisui Plastics Co. Ltd., Tokyo, Japan
Calcium acetate ($Ca(CH_3COO)_2 \cdot H_2O$)	0.194	Wako Pure Chemicals Industries Ltd., Osaka, Japan
Benzoyl peroxide (BPO)	0.029	Wako Pure Chemical Industries Ltd., Osaka, Japan
Barium sulfate ($BaSO_4$)	0.097	Sakai Chemical Industry Co. Ltd., Osaka, Japan
Liquid		
Methylmethacrylate (MMA) monomer	0.397	Wako Pure Chemical Industries Ltd., Osaka, Japan
N,N-dimethyle-p-toluidine (NDT)	0.004	Kanto Chemical Co. Inc., Tokyo, Japan
γ-Methacryloxypropyl-trimethoxysilane (MPS)	0.099	Chisso Industry Co. Ltd., Tokyo, Japan

(FE-SEM, S-4700, Hitachi Co., Tokyo, Japan) and surface roughness tester (SV-3000S4, Mitutoyo Co., Japan).

2.5. Animal study

Hardened cylindrical specimens (15 mm in length and 4 mm in diameter) of the cements were subjected to implantation for mechanical test. The specimens were implanted into the femur of nine 2-year-old female beagle dogs weighing 8–11 kg. The guidelines for animal experimentation of Chiba University were carefully observed. They were sedated with an intramuscular injection of Ketamine chloride (10 mg/kg). The cylindrical specimen was inserted into each femur of the dog from the lateral aspect of the diaphysis hemicortically. Specimens were randomly distributed in the femur sites to avoid a positional bias. For histological study, we used six 2-year-old female beagle dogs weighing 8–11 kg. Through the parapatellar approach to the distal femur, the medullary cavity was drilled from this region and intramedullary injection of the cement solutions into the dog femur was performed manually using 20 ml syringe. Icepacin sulfate (200 mg) was administered intramuscularly just before the operation. After the operation, the animals were housed in cages, provided with water and chow, and allowed to move unrestricted at all times. After 3, 5 and 8 weeks, the dogs were sacrificed with an overdose of sodium pentobarbital. The femur with the inserted specimen was removed. The strength of the implant–bone interface was evaluated for six specimens at each determination point using the push-out test. The prepared fresh samples were fixed in a testing jig with resin, and the implants were pushed out from the surrounding bone using a material testing machine (SHIMADZU EHF-F01, Shimadzu Co., Kyoto, Japan) [13]. A loading rate of 0.5 mm/min was used for all tests. A load–displacement curve was recorded to measure the maximum force at breakage, which was defined as the bonding strength between bone and the implant. For the histological study, the dog femur with hardened injected cement was transversely sectioned at the diaphysis. Two samples were examined at each determination point. The interface between cement and bone was also observed by micro-focus X-ray computed tomography (micro-CT; MCT-CB130MF, Hitachi medical Co., Japan). The samples were soaked in 70 mass% ethanol solution for fixation. They were dehydrated by consecutive soaking for 1 day in each solution of a graded ethanol/water system (ethanol/water: 70/30, 80/20, 90/10, 95/5, 97/3, and 100/0 in mass ratio). The dried specimens were embedded in epoxy resin. A 200-μm cross-section was cut from the specimen and mounted on a slide glass, followed by polishing to a thickness of approximately 30 μm. Toluidine blue staining and Villannueva–Goldner staining were performed to observe the surrounding bone reaction under an optical microscope. For the histological study, calcified bone in the interstices between cortex bone and cement surface were measured by analyzing software Winroof® (Mitani Co., Japan) at 8 weeks. Regions of interest (ROIs) were defined as exactly the same size (1.1 mm × 1.1 mm) in all samples and two regions of each sample were measured.

2.6. Statistical analysis

Values were expressed as the mean±standard deviation (SD). Statistical differences were analyzed with the use of the Mann Whitney U test; $p<0.05$ was considered statistically significant. Two of the specimens for push-out test were infected and four specimens were implanted incorrectly. So we discarded these specimens, and the final numbers (n) were 6, 3 and 4 for modified PMMA and 6, 4 and 5 for conventional one at 3, 5 and 8 weeks after implantation, respectively.

3. Results

Table 2 gives the maximum temperature during setting of the bone cements and their setting time. The setting time of the modified cement was longer than that of conventional PMMA bone cement (Zimmer® bone cement), while

Table 2
Maximum temperature during polymerization and setting time

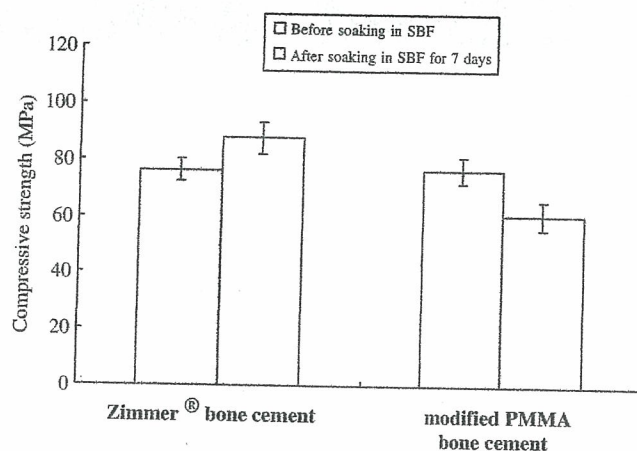| Sample	Maximum temperature (°C, mean±SD)	Setting time (min, means±SD)
Zimmer® bone cement	82.5±0.6	12.0±0.4
Modified PMMA bone cement	51.0±1.2	18.1±2.3

Fig. 1. The compressive strength of the cements with or without exposure to simulated body fluid (SBF).

the maximum temperature during the setting of the modified cement was lower. Fig. 1 shows the compressive strength of the cements with or without soaking in SBF for 7 days. The compressive strength of the modified cement without soaking in SBF was almost the same as the conventional one, but when soaked in SBF, it decreased and did not satisfy the value required by ISO5833 (70 MPa). Fig. 2 shows SEM photographs of the surface of the cements before and after soaking in SBF for various periods. Aggregations of tiny particles were newly observed on the surface of the modified cement soaked in SBF for 1 day, whereas no significant changes were observed on the surface of the Zimmer® bone cement. Fig. 3 shows TF-XRD patterns of the cements with and without soaking in SBF for various periods up to 7 days. Peaks assigned to hydroxyapatite (JCPDS#15-0876) with low crystallinity were detected approximately at $2\theta = 32°$ for modified cement, while Zimmer® bone cement showed peaks assigned to barium sulfate (JCPDS#24-1035). These results indicate that the apatite crystals with fine particles were deposited on the surface of the modified cement within 1 day after soaking in SBF, to form a layer of hydroxyapatite on the modified cement. In contrast, Zimmer® bone cement did not show any apatite formation after exposure to SBF. Table 3 shows surface roughness of the cements with and without soaking in SBF for 1, 3 and 7 days. Surface roughness (Ra) of the modified PMMA bone
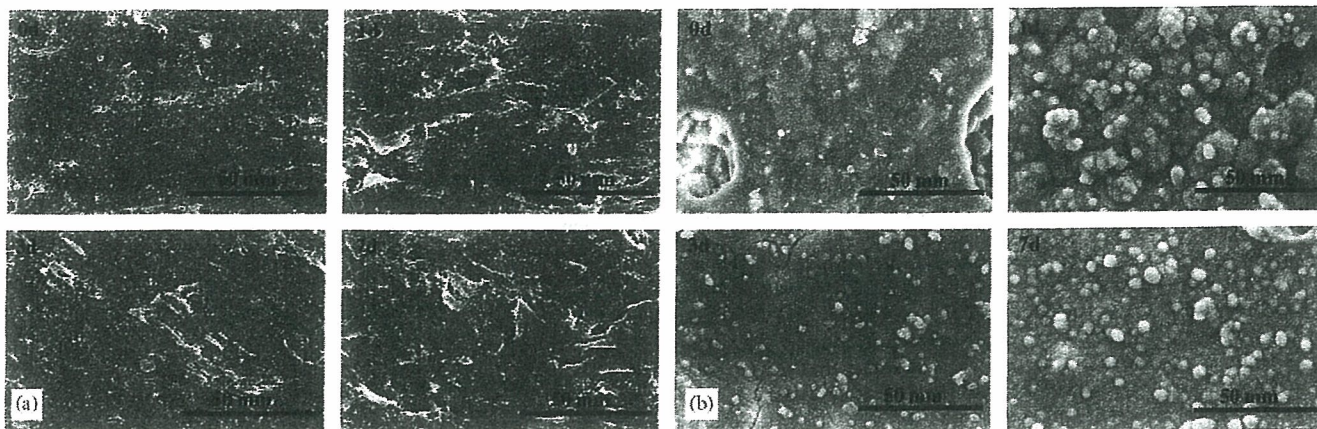
Fig. 2. SEM photographs of the surfaces of (a) Zimmer® bone cement and (b) the modified PMMA bone cement, after soaking in simulated body fluid (SBF) for 1, 3 and 7 days. "0d" indicates the specimen without soaking in SBF.
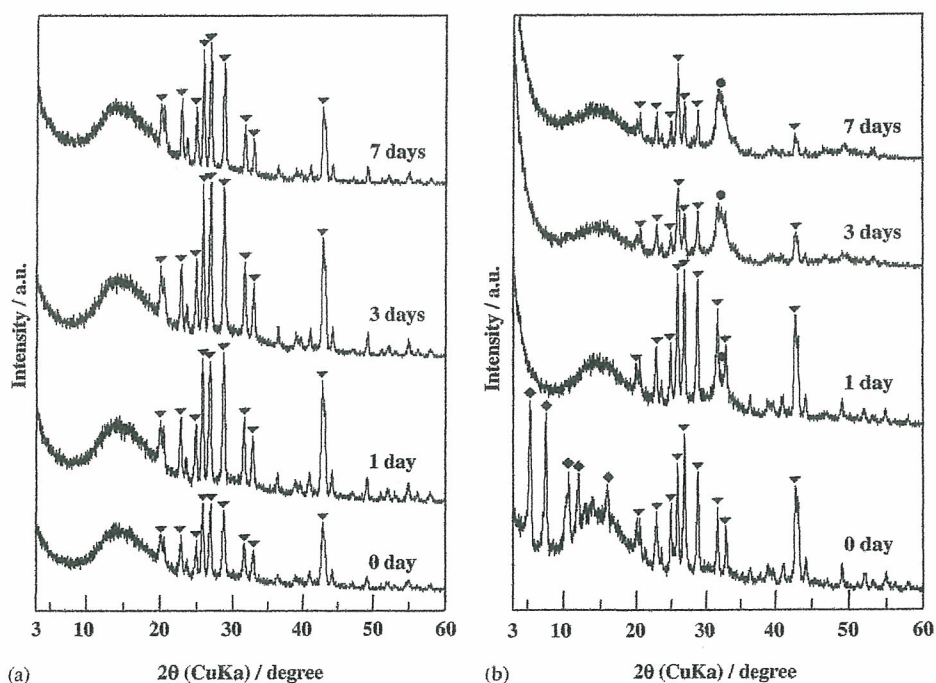

Fig. 3. TF-XRD patterns of the cements with and without soaking in simulated body fluid (SBF) for 1, 3 and 7 days. "0 day" indicates the specimen without soaking in SBF. Black circle: hydroxyapatite (JCPDS#15-0876); black triangle: barium sulfate (JCPDS#24-1035); black diamond: calcium acetate · 0.5H$_2$O (JCPDS#19-0199): (a) Zimmer® bone cement and (b) modified PMMA bone cement.

Table 3
Surface roughness of cements (Ra; mm) with and without soaking in simulated body fluid (SBF) for 1, 3 and 7 days

Sample	Surface roughness of cements (Ra;mm)			
	0 day	1 day	3 days	7 days
Zimmer® bone cement	0.729±0.09	0.882±0.23	0.576±0.08	0.681±0.05
Modified PMMA bone cement	0.316±0.05	1.023±0.10	1.297±0.24	3.385±0.30

cement distinctly increased with increasing soaking periods in SBF, whereas Zimmer® bone cement did not.

Fig. 4 shows the results of push-out test after 3, 5 and 8 weeks implantation of the modified PMMA bone cement, in comparison with those of Zimmer® bone cement. Although the condition differed from the actual clinical application in which the cement is inserted before setting, a significantly higher binding strength ($p < 0.05$) was

observed for the modified PMMA bone cement than Zimmer® bone cement, at each implantation period. The push-out load of the modified PMMA bone cement reached 1.60 MPa in 3 weeks, which was maintained up to 8 weeks after implantation, while those of Zimmer® bone cement remained low throughout the examined periods in this study. Thi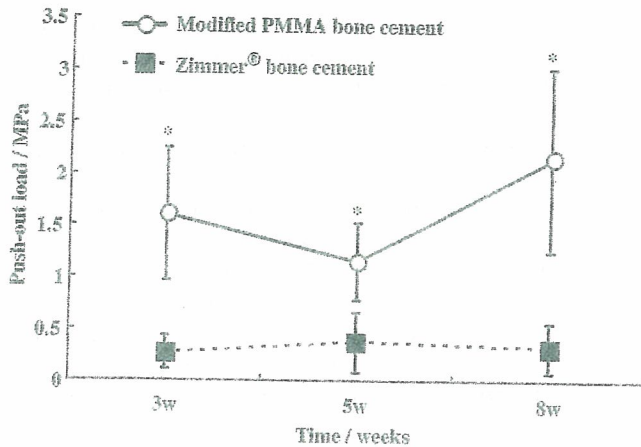s result clarifies that the modified PMMA bone cement results in tight fixation with greater strength than conventional PMMA bone cement. In the area where there was a gap between the bone cortex and the surface of modified PMMA, micro-CT and microscopic images showed new bone formation and lamellar bone bridges in all animals 8 weeks after implantation (Fig. 5). On the other hand, little new bone formation was observed for the Zimmer® bone cement. Fig. 6 shows the percentage fraction of the calcified bone in the interstices between cortex bone and cement surface measured by the analyzing software Winroof® in 8 weeks' samples. The percentage fraction of the calcified bone around the modified PMMA bone cement was significantly larger than Zimmer® bone cement ($p = 0.02$). These evidences support the finding that the higher strength on the push-out test for modified PMMA is attributed to higher affinity, which is osteoconduction, of the modified PMMA bone cement to bone than that of the conventional PMMA bone cement.

Fig. 4. Results of push-out strength after implantation in dog femur. A significantly higher binding strength ($p < 0.05$) was observed for the modified PMMA bone cement compared to Zimmer® bone cement (conventional PMMA bone cement), at each implantation period.

4. Discussion

To develop a bioactive PMMA-based bone cement, an optimal composition was sought to obtain adequate mechanical strength and handling properties. Additives for inducing bioactivity on bone cement should not affect the workability of the bone cement. Previous reports on modifications of PMMA bone cement with MPS and
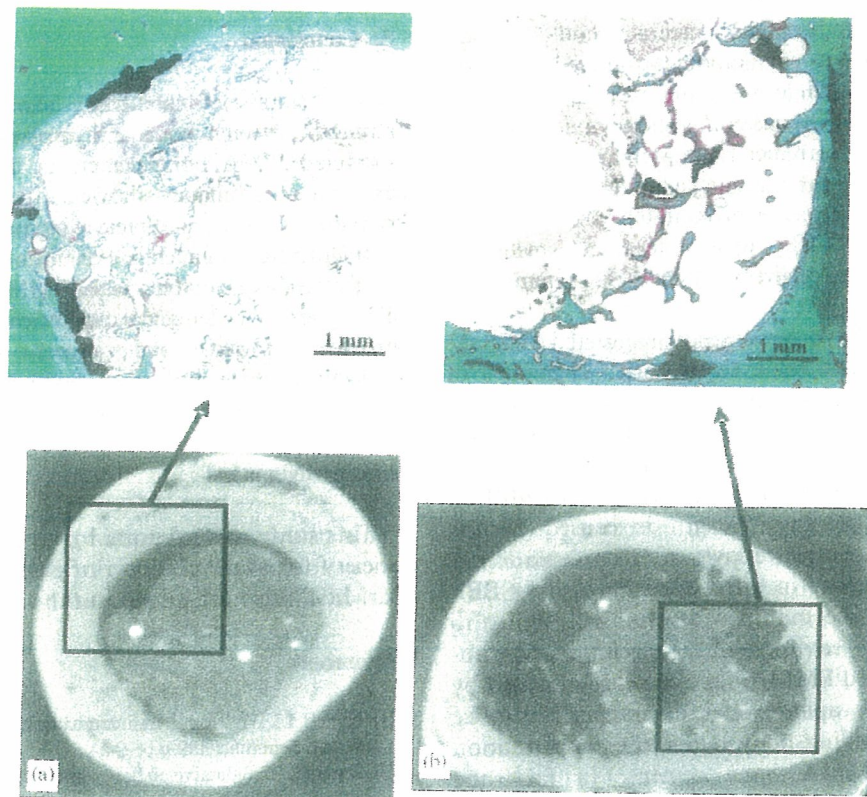

Fig. 5. Images of micro-focus X-ray computed tomograms (micro-CT) at 8 weeks after implantation, in comparison with microscopic images (Villannueva–Goldner stain × 1): (a) Zimmer® bone cement and (b) modified PMMA bone cement.
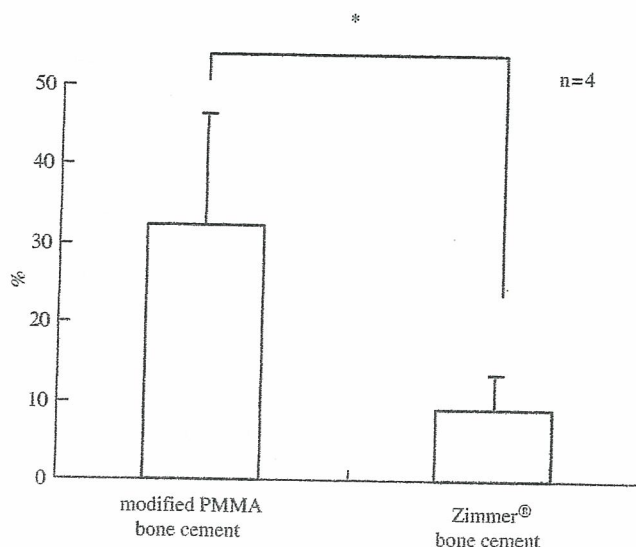
Fig. 6. Results of the percentage fraction of the calcified bone in the interstices between cortex bone and cement surface at 8 weeks. More calcified bone (*$p < 0.05$) was observed for the modified PMMA bone cement compared to Zimmer® bone cement (conventional PMMA bone cement). Measured by analyzing software Winroof® ($n = 4$).

calcium salts showed prolonged setting time and reduced mechanical strength after the modification [8,14]. These problems can be solved by selecting the appropriate calcium salts [10]. In this study, it was confirmed that MPS and heat-treated calcium acetate could be the appropriate candidates for modification, because the setting time was within 20 min and there was minimal heat generation during polymerization as shown in Table 2. Incorporation of MPS reduced the polymerization rate, compared to MMA liquid alone. The reduction in the compressive strength from approximately 75 to 65 MPa due to exposure to SBF, which does not meet the mechanical properties required by ISO 5833, remains a problem to be solved.

The findings of the present study suggested that the modification of PMMA bone cement with 20 mass% of MPS and calcium acetate resulted in high biological affinity to living bone. Thus, a higher binding strength could be achieved between the modified PMMA bone cement and living bone than for the conventional PMMA bone cement. The binding strength is caused by the formation of a hydroxyapatite layer after implantation in the bony defect, because in vitro evaluation using SBF clearly showed that the modified cement had ability to form apatite in body environment. Therefore, osteoconduction of the modified PMMA bone cement is induced by the formation of the apatite layer through the surface reaction with surrounding body fluids after implantation of the modified PMMA bone cement. In fact, the animal study indicated that there was extensive new bone formation around the modified PMMA bone cement, and that direct bone apposition to the modified PMMA bone

cement surface was observed on histological examination. Micro-CT images also showed bridges of new bone from the bone cortex to the surface of the modified PMMA bone cement that had developed into lamellar bone 8 weeks after implantation. This in vivo evidence confirms the fact that modified PMMA bone cement has higher affinity to living bone tissue, than the conventional PMMA bone cement. In contrast, conventional PMMA bone cement is more stable in chemical reaction to body fluids than the modified one. The stability of the conventional PMMA bone cement in body environment is confirmed from the results of TF-XRD, SEM and surface roughness, as seen in Figs. 2 and 3 as well as Table 3. Although the modifications with MPS and calcium acetate make the PMMA bone cement bioactive, dissolution of the components, probably calcium acetate and part of hydrolyzed MPS, results in a decrease in compressive strength of the cement as shown in Fig. 1. The increase in the surface roughness of the modified PMMA bone cement shown in Table 3 is attributed to dissolution of the calcium acetate from the bone cement and/or deposition of apatite crystals, through reaction of the cement with SBF. Increased surface roughness may contribute to an increase in binding strength between the cement and living bone due to anchoring effects. On the other hand, the toxicity of the dissolved components should be clarified in future studies. Long-term stability after implantation should be clarified in order to achieve successful application.

5. Conclusion

The results of this study show that higher bonding strength between bone and implant can be achieved with modified PMMA bone cements. Histological observation and micro-CT images showed that the PMMA cement modified with γ-methacryloxypropyl trimethoxysilane (MPS) and calcium acetate exhibits osteoconductive properties, whereas the conventional PMMA bone cement did not. This type of chemical modification was effective in providing PMMA bone cement with bioactivity, thus developing a new bioactive bone cement with a potential for much stable fixation in a short period after implantation.

References

[1] Hench LL, Wilson J. An introduction to bioceramics. Singapore: World Scientific; 1993. p. 1–24.

[2] Harper EJ. Bioactive bone cements. Proc Inst Mech Eng H 1998;212:113–20.

[3] Shinzato S, Kobayashi M, Mousa WF, Kamimura M, Neo M, Kitamura Y, et al. Bioactive polymethylmethacrylate-based bone cement: comparison of glass beads, apatite- and wollastonite-containing

glass–ceramic, and hydroxyapatite fillers on mechanical and biological properties. J Biomed Mater Res 2000;51:258–72.

[4] Shinzato S, Nakamura T, Kokubo T, Kitamura Y. A new bioactive bone cement: effect of glass bead filler content on mechanical and biological properties. J Biomed Mater Res 2001; 54:491–500.

[5] Kokubo T. Recent progress in glass-based materials for biomedical applications. J Ceram Soc Japan 1991;99:965–73.

[6] Kim HM. Bioactive ceramics: challenges and perspectives. J Ceram Soc Japan 2001;109:S49–57.

[7] Ohtsuki C, Kokubo T, Yamamuro T. Mechanism of apatite formation on CaO–SiO$_2$–P$_2$O$_5$ glasses in a simulated body fluid. J Non-Cryst Solids 1992;143:84–92.

[8] Ohtsuki C, Miyazaki T, Kyomoto M, Tanihara M, Osaka A. Development of bioactive PMMA-based cement by modification with alkoxysilane and calcium salt. J Mater Sci Mater Med 2001; 12:895–9.

[9] Mori A, Ohtsuki C, Miyazaki T, Sugino A, Tanihara M, Kuramoto K, et al. Synthesis of bioactive PMMA bone cement via modification with methacryloxypropyltrimethoxysilane and calcium acetate. J Mater Sci Mater Med 2005;16:713–8.

[10] Mori A, Ohtsuki C, Miyazaki T, Sugino A, Tanihara M, Kuramoto K, et al. Synthesis of bioactive PMMA bone cement via modification with methacryloxypropyltrimethoxysilane and calcium acetate. J Mater Sci Mater Med 2005;16:713–8.

[11] ISO. International standard 5833/2: implants for surgery acrylic resin cements. Orthopaedic application, 1992.

[12] Kokubo T, Kushitani H, Sakka S, Kitsugi T, Yamamuro T. Solutions able to reproduce in vivo surface-structure changes in bioactive glass ceramic A-W. J Biomed Mater Res 1990;24:721–34.

[13] Nishimura N, Taguchi T, Yamamuro T, Nakamura T, Kokubo T, Yoshihara S. A study of the bioactive bone cement–bone cement interface: quantitative and histological evaluation. J Appl Biomater 1993;4:29–38.

[14] Miyazaki T, Ohtsuki C, Kyomoto M, Tanihara M, Mori A, Kuramoto K. Bioactive PMMA bone cement prepared by modification with methacryloxypropyltrimethoxysilane and calcium chloride. J Biomed Mater Res 2003;67A:1417–23.

A PEG-Based Biocompatible Block Cationer with High Buffering Capacity for the Construction of Polyplex Micelles Showing Efficient Gene Transfer toward Primary Cells

Naoki Kanayama,[a, d] Shigeto Fukushima,[a, c] Nobuhiro Nishiyama,*[b] Keiji Itaka,[b] Woo-Dong Jang,[a] Kanjiro Miyata,[a] Yuichi Yamasaki,[a, d] Ung-il Chung,[b] and Kazunori Kataoka*[a, b, d]

Nonviral gene vectors from synthetic cationers (polyplexes) are a promising alternative to viral vectors. In particular, many recent efforts have been devoted to the construction of biocompatible polyplexes for in vivo nonviral gene therapy. A promising approach in this regard is the use of poly(ethylene glycol) (PEG)-based block cationers, which form a nanoscaled core–shell polyplex with biocompatible PEG palisades. In this study, a series of PEG-based block cationers with different amine functionalities were newly prepared by a simple and affordable synthetic procedure based on an aminolysis reaction, and their utility as gene carriers was investigated. This study revealed that the block cationers carrying the ethylenediamine unit at the side chain are capable of efficient and less toxic transfection even toward primary cells, highlighting critical structural factors of the cationic units in the construction of polyplex-type gene vectors. Moreover, the availability of the polyplex micelle for transfection with primary osteoblasts will facilitate its use for bone regeneration in vivo mediated by nonviral gene transfection.

Introduction

Gene therapy is a promising approach for the treatment of genetic and intractable diseases and for tissue engineering; however, its success still strongly depends on the development of useful gene vectors.[1] Recently, nonviral vectors based on the complexation of plasmid DNA (pDNA) with synthetic cationic polymers (cationers) have attracted a great deal of attention as an alternative to viral vectors.[2–4] These vectors, the so-called polyplexes, are aimed toward both efficient transfection and decreased cytotoxicity.[5,6] In particular, there has recently been a strong impetus toward engineering the constituent cationers to construct biocompatible polyplexes suitable for gene delivery in vivo.[2,5] A promising approach in this regard is the block copolymerization of cationers with poly(ethylene glycol) (PEG) to obtain PEG-*block*-cationers, as they spontaneously associate with pDNA to form polyplex micelles at the sub-100-nm scale with a dense and hydrophilic PEG palisade surrounding the polyplex core (Figure 1).[7–10] These polyplex micelles with PEG palisades showed high colloidal stability under physiological conditions and afforded appreciable levels of reporter-gene expression to various cell lines even after preincubation in a serum-containing medium.[7] Notably, the polyplex micelles demonstrated longevity in blood circulation,[11] offering the possibility of their use in systemic gene delivery. Nevertheless, a major obstacle to the successful application of this biocompatible nonviral vector system remains: the limited transfection efficacy toward primary cells.

Herein, we report a novel approach to obtain PEG-*block*-cationers with remarkably high transfecting activity even toward primary cells, which are known to be sensitive to the toxicity induced by conventional polyplexes. The synthetic strategy for novel block cationers is based on our unprecedented finding that the flanking benzyl ester groups of poly(β-benzyl L-aspar-

[a] Dr. N. Kanayama, S. Fukushima, Dr. W.-D. Jang, K. Miyata, Dr. Y. Yamasaki, Prof. Dr. K. Kataoka
Department of Materials Engineering
Graduate School of Engineering
The University of Tokyo
Tokyo 113-8656 (Japan)
Fax: (+81)3-5841-7139
E-mail: kataoka@bmw.t.u-tokyo.ac.jp

[b] Dr. N. Nishiyama, Dr. K. Itaka, Prof. Dr. U.-i. Chung, Prof. Dr. K. Kataoka
Center for Disease Biology and Integrative Medicine
Graduate School of Medicine
The University of Tokyo, Tokyo 113-0033 (Japan)
Fax: (+81)3-5841-7139
E-mail: nishiyama@bmw.t.u-tokyo.ac.jp

[c] S. Fukushima
R&D Division, Pharmaceuticals Group
Nippon Kayaku Co., Ltd. (Japan)

[d] Dr. N. Kanayama, Dr. Y. Yamasaki, Prof. Dr. K. Kataoka
Core Research for Evolutional Science and Technology (CREST), Japan
Science and Technology Agency (JST) (Japan)

Supporting information for this article is available on the WWW under
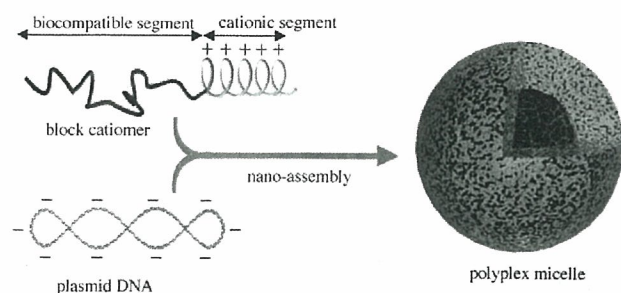http://www.chemmedchem.org or from the author.

Figure 1. Formation of polyplex micelles through the electrostatic interaction between block catiomers and plasmid DNA.

tate) (PBLA) can undergo a quantitative aminolysis reaction with various polyamine compounds under mild anhydrous conditions at 40 °C, thus allowing the preparation of cationic polyaspartamides with different amine functionalities, yet with the same molecular weight and distribution (Scheme 1). In par-
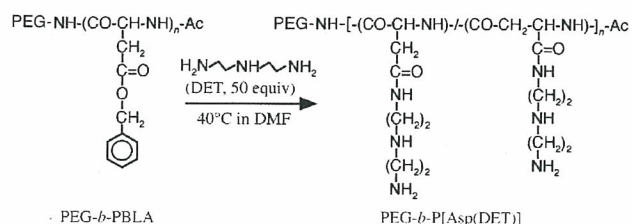
Scheme 1. Synthesis of PEG-*b*-P[Asp(DET)] block catiomer through the aminolysis of PEG-*b*-PBLA. DMF = *N,N*-dimethylformamide.

ticular, this study is focused on the unique properties of the ethylenediamine unit integrated into the polyaspartamide side chain. Notably, ethylenediamine is known to undergo a clear two-step protonation with a distinctive *gauche–anti* conformational transition as depicted in Scheme 2,[12] and is thus expected to provide an effective buffering function in the acidic en-
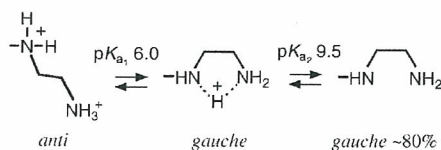
Scheme 2. Two-step protonation of the ethylenediamine unit with a distinctive *gauche–anti* conformational transition.

dosomal compartment (pH 5). It has been suggested that catiomers with a low pK_a value such as polyethylenimine could buffer endosomal acidification and cause an increase in osmotic pressure in the endosome, leading to the disruption of the endosomal membrane to facilitate polyplex transport into the cytoplasm (the so-called proton sponge effect[13]). Indeed, PEG-*block*-polyaspartamide with an ethylenediamine unit at the side chain (PEG-*b*-P[Asp(DET)]) showed a remarkably high transfection efficacy to various cancer cells as well as mouse primary osteoblast cells. Importantly, this block catiomer was

found to have remarkably low toxicity, facilitating its use for in vivo gene therapy.

Results and Discussion

PEG-*b*-polyaspartamide carrying the *N*-(2-aminoethyl)aminoethyl group $-(CH_2)_2NH(CH_2)_2NH_2$ as the side chain (PEG-*b*-P[Asp(DET)]) was prepared by the aminolysis of PEG-*b*-PBLA in dry DMF at 40 °C for 24 h in the presence of a molar excess (50 equiv relative to benzyl groups) of diethylenetriamine (DET) (Scheme 1). The ^{1}H NMR spectrum of PEG-*b*-P[Asp(DET)] is shown in Figure 2, and the ^{13}C NMR spectrum is available in
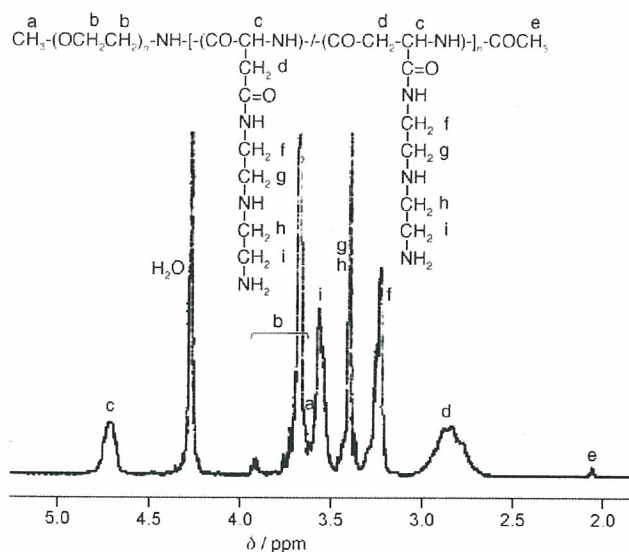

Figure 2. ^{1}H NMR spectrum of PEG-*b*-P[Asp(DET)] (solvent: D_2O, $T = 80$ °C); the polymer is in a salt form.

the Supporting Information. These data indicate that the aminolysis of the PBLA benzyl groups proceeded in a selective manner to the primary amine moiety of DET. Also, comparison of the integration ratio of the proton peaks (b and f–i) in Figure 2 reveals quantitative introduction of DET into the side chain of PBLA, and a unimodal molecular weight distribution of the obtained polymer was revealed by size-exclusion chromatography (SEC) measurement (Supporting Information). These results suggest a minimal occurrence of inter- or intrapolymer cross-linking by DET during aminolysis. Note that the peaks from the carbonyl and methylene groups of the aspartamide units in the ^{13}C NMR spectrum (Figure S1, Supporting Information) are split into two peaks, suggesting that the aminolysis of PBLA might induce intramolecular isomerization of the aspartamide units to form β-aspartamide. Figure 3 shows the time course of the aminolysis reaction of PBLA with DET, which was evaluated from the change in the ratio of the proton peak integration (f over b) in the ^{1}H NMR spectrum (Figure 2). This result indicates a fast and quantitative aminolysis of PBLA, which is in marked contrast to the lack of aminolysis with poly(γ-benzyl L-glutamate) (PBLG) under the same re-
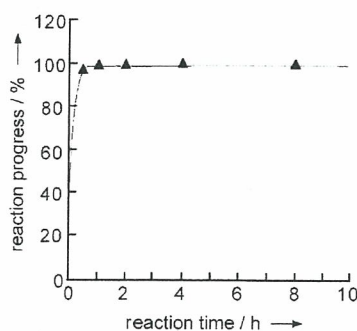
Figure 3. Time course of the aminolysis of PEG-*b*-PBLA with DET in DMF at 40 °C. The reaction progress was estimated from the change in the ratio of the proton peak integration (f over b) in the ¹H NMR spectrum (Figure 2).

action conditions (data not shown), highlighting a unique mechanism involved in the aminolysis of PBLA under mild conditions. Presumably, the amide groups of the main chain interact with the carbonyl group of the side chain, which may facilitate the aminolysis reaction.[14] The details of the mechanism of this unique aminolysis reaction are now under investigation in our research group and will be reported elsewhere.

The pH-dependent protonation of PEG-*b*-P[Asp(DET)] in media containing 150 mM NaCl was evaluated by potentiometric titration. The α/pH curve shown in Figure 4 clearly indicates
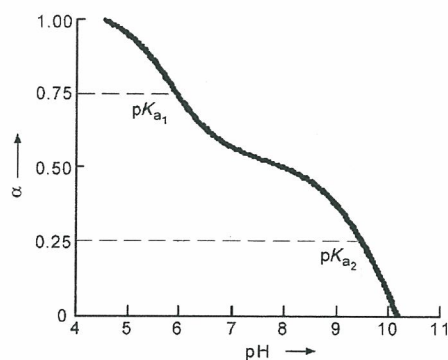

Figure 4. Degree of protonation (α) as a function of pH (α/pH curve) for the PEG-*b*-P[Asp(DET)] block catiomer (150 mM NaCl, aq, 25 °C).

the two-step protonation behavior of PEG-*b*-P[Asp(DET)], which is attributable to the two-step protonation of the ethylenediamine moiety with a distinctive *gauche–anti* conformational transition as indicated in Scheme 2. The two distinct pK$_a$ values of the ethylenediamine moiety in the side chain of polyaspartamide were determined to be 6.0 and 9.5. Notably, this group remains nearly 100% populated by the mono-protonated state (*gauche* form) at pH 7.4, and is capable of exerting a substantial buffering effect in the pH range down to 5.0, at which point the equilibrium shifts to the di-protonated state (*anti* form) (Scheme 2).

The polyplex micelle was prepared by mixing solutions of PEG-*b*-P[Asp(DET)] and pDNA in various ratios of *N/P*, for which *N* is the total number of amine groups in the block catiomer

and *P* represents the number of phosphate units in the pDNA. The formation of the polyplex, which accompanies pDNA condensation, was followed by an ethidium bromide (EtBr) dye-exclusion assay at different pH values. As shown in Figure 5, the
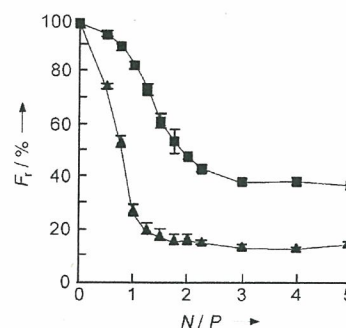

Figure 5. Effect of pH (▲: pH 5.0, ■: pH 7.4) on the relative fluorescence intensity (F_r) of EtBr in solution with pDNA and PEG-*b*-P[Asp(DET)] at various *N/P* ratios.

fluorescence intensity of EtBr decreases with an increase in the *N/P* ratio. At pH 5.0, the fluorescence of EtBr levels off at *N/P*= 1, which is consistent with approximately 95% protonation of the ethylenediamine unit, as expected from the α/pH curve in Figure 4. On the other hand, at pH 7.4, substantial quenching occurred at *N/P*≈2.0, which is consistent with the hypothesis that the mono-protonated form of the ethylenediamine unit in PEG-*b*-P[Asp(DET)] might be maintained even inside the polyplex. It is possible that the stabilized *gauche* conformation (Scheme 2) of the mono-protonated form may prevent the ethylenediamine unit from further protonation facilitated by the zipper effect or the local electrostatic field effect in the complexation process with anionic pDNA at pH 7.4.[15] The cumulant diameters and ζ potentials of the polyplexes prepared at different *N/P* ratios are shown in Figure 6. The cumulant diameters of the polyplex micelles were determined to be 70–90 nm throughout the range of the examined *N/P* ratios of 1–20, and the ζ potentials of the polyplexes increased with *N/P* ratios and leveled off at *N/P*= 2 (Figure 6). At *N/P*>2, the polyplexes were observed to have small absolute ζ potentials (~8 mV), suggesting a core–shell architecture with a hydrophilic and neutral PEG shell surrounding the polyplex core.
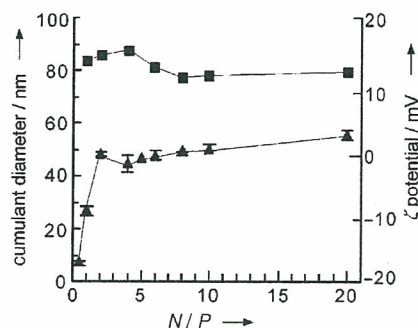
Figure 6. Cumulant diameter (■) and ζ potential (▲) of the PEG-*b*-P[Asp(DET)] polyplex micelles as a function of *N/P* ratio.

The in vitro transfection efficiency (TE) against human hepatoma HuH-7 cells was assessed by a luciferase assay (Figure 7). Notably, a similar trend in TE was also observed for human kidney 293T cells (Supporting Information). In this experiment,
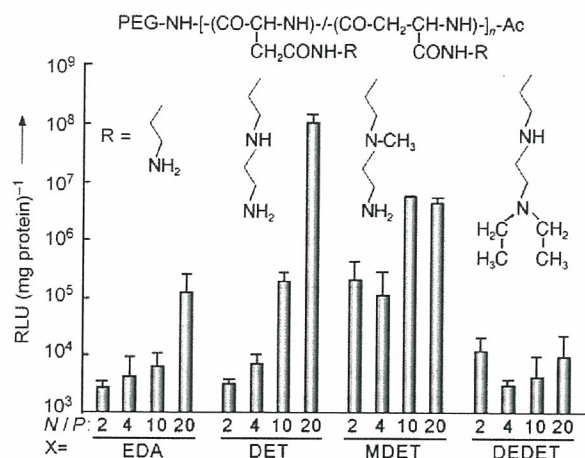

Figure 7. In vitro transfection of the luciferase gene into HuH-7 cells by polyplex micelles from PEG-*b*-polyaspartamides carrying various polyamine components in the side chain (PEG-*b*-P[Asp(X)]) with varying *N/P* ratios. Transfection is reported in relative light units (RLU) per mg protein. The cells were incubated with each polyplex in the medium containing 10% serum for 24 h, followed by incubation for a further 24 h in the absence of polyplex.

the PEG-*b*-P[Asp(DET)]–pDNA micelle was compared with the polyplex micelles from various PEG-*b*-polyaspartamide catiomers made by the similar aminolysis of PEG-PBLA with different amine compounds, with the aim to highlight the unique nature of the P[Asp(DET)] segment. Note that the polyplex micelles from each block catiomer prepared in this study showed sizes and ζ potentials similar to those of the polyplex micelle from PEG-*b*-P[Asp(DET)] (data not shown). The polyplex micelle from the block catiomer with the 2-aminoethyl group —$(CH_2)_2NH_2$ (pK_a 9.4) in the side chain (PEG-*b*-P[Asp(EDA)]), which was prepared through the aminolysis of PEG-*b*-PBLA with ethylenediamine (EDA), showed only 1/10000 of the TE compared with the PEG-*b*-P[Asp(DET)] polyplex micelle at *N/P* = 20. This is presumably due to the impaired buffering capacity of the —$(CH_2)_2NH_2$ unit with the high pK_a value of 9.4 in the experimental pH range as well as to the weak ability of PEG-*b*-P[Asp(EDA)] to condense pDNA based on the EtBr exclusion assay (data not shown).

The TE of the PEG-*b*-P[Asp(DET)] polyplex micelle was further compared with those of the polyplex micelles from the PEG-*b*-polyaspartamide catiomers carrying the N-alkylated ethylenediamine units in the side chain to explore the structural features of the polyplex micelles that are important for effective gene transfection (Figure 7). These block catiomers, PEG-*b*-P[Asp(MDET)] and PEG-*b*-P[Asp(DEDET)], are prepared by the aminolysis reaction of PEG-PBLA with the corresponding amine compounds, 4-methyldiethylenetriamine (MDET) and *N,N*-diethyldiethylenetriamine (DEDET), respectively. Both the PEG-*b*-P[Asp(MDET)] and PEG-*b*-P[Asp(DEDET)] polyplex micelles

showed an appreciably lower TE than the PEG-*b*-P[Asp(DET)] polyplex micelle, particularly at higher *N/P* ratios (Figure 7). This result, which highlights the critical sensitivity of TE toward subtle changes in catiomer structure, indicates that additional structural factors, besides distinct pK_a values, play a substantial role in determining the TE of the polyplex micelles constructed from the PEG-*b*-polyaspartamide catiomers carrying the derivatized ethylenediamine units as a side chain; further study is needed to clarify the detailed mechanisms.

The cytotoxicity of the polyplex-forming catiomers is also a crucial aspect for successful nonviral gene therapy. In this regard, all the polyplex micelles from each block catiomer shown in Figure 7 elicited no appreciable cytotoxicity toward HuH-7 cells under the same conditions used for gene transfection (data not shown). Notably, the polyplex micelle from PEG-*b*-P[Asp(DET)] showed remarkably low cytotoxicity despite its efficiency in gene transfection. Therefore, the intrinsic cytotoxicity of PEG-*b*-P[Asp(DET)] catiomer was further assessed against HuH-7 cells, and compared with that of branched polyethylenimine (BPEI, 25 kDa, Aldrich Chemical, USA) and linear polyethylenimine (LPEI, 22 kDa, ExGen500, MBI Fermentas, Germany). As shown in Figure 8, the PEG-*b*-P[Asp(DET)] catiomer showed > 20-fold higher 50% growth-inhibitory concentration (IC_{50}) than BPEI and LPEI, highlighting the remarkably low cytotoxicity of the block catiomers synthesized in this study.
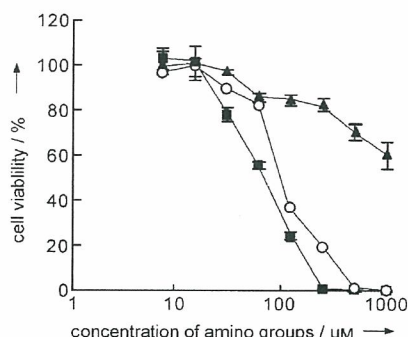
Figure 8. Cytotoxicity of branched (BPEI, ○) and linear (LPEI, ■) polyethylenimines and PEG-*b*-P[Asp(DET)] (▲) against HuH-7 cells. The cells were incubated with each catiomer with different concentrations for 48 h.

The major challenge for the practical use of synthetic vectors in gene therapy is the effective and non-cytotoxic gene transfer to primary cells with therapeutic interest. To evaluate the feasibility of the PEG-*b*-P[Asp(DET)] polyplex micelles toward such primary cells, mouse primary osteoblasts, which are the focus of clinical interest in bone regeneration,[16] were challenged with the polyplex micelles. The luciferase plasmid was transfected, and the resulting TE and cytotoxicity profiles are shown in Figure 9. Notably, the PEG-*b*-P[Asp(DET)] system with *N/P* = 80 gave a TE similar to the polyplexes from ExGen500, the most effective transfection reagent based on LPEI,[17] with the optimal *N/P* ratios (Figure 9A). Nonetheless, the PEG-*b*-P[Asp(DET)] system exhibited no appreciable cytotoxicity under the conditions of gene transfection (Figure 9B).